

middle of a 50-mm-thick host cell are shown in Fig. 2, A and B. Because the scattering loss from the water droplet is less than that from the surrounding host, the intensity of the projected image of the water droplet was brighter than that of the host. The shape of these water droplets depends on the amount of water released. The delay time between the stopper opening and the photographic time was varied from ~ 2 to 10 s. The inhomogeneity of the brighter circle in Fig. 2 that corresponds to the collection aperture or signal beam diameter of ~ 12.7 mm was accounted for by the nonuniformity of the laser intensity distribution.

To determine the contrast of the transmitted early snake light images as shown in Fig. 3, four different phantom droplets with 1, 2, 3, and 5% diluted Intralipid solutions were dropped into a 2% host medium. The projected image from the 5% Intralipid droplet shown in Fig. 3D is the darkest because of the increased scattering from the droplet, while the projected image from the 2% Intralipid droplet shown in Fig. 3B is hardly distinguishable from the surrounding host with the identical scattering property. The image obtained from the 1% Intralipid droplet (Fig. 3A) is brighter and the image from the 3% Intralipid droplet in Fig. 3C is darker than that from the 2% surrounding host. A 1% concentration dilution difference between the phantom droplet and the host medium can be distinguished visually. The changes of the shape of the drop can be measured. A much smaller concentration difference of 0.1% between the phantom droplets and the host medium could be identified with digital video signal processing (10). This work demonstrates that small differences in scattering properties and the shapes of small dimension translucent droplets can be spatially determined inside a large host turbid medium that may be useful in moving toward the optical mammography. A droplet phantom inside a scattering host without an artificial container boundary is an ideal object to simulate, for example, a tumor embedded in a tissue or droplets in jet exhaust. Furthermore, the early light transillumination technique can be adapted to determine the spatial distribution of the particle size and shape of the fuel spray in air from a jet nozzle to improve efficient engine design.

REFERENCES AND NOTES

1. L. Wang, P. P. Ho, C. Liu, G. Zhang, R. R. Alfano, *Science* **253**, 769 (1991).
2. M. A. Duguay and A. T. Mattick, *Appl. Opt.* **10**, 2162 (1971).
3. L. Wang, P. Ho, X. Liang, H. Dai, R. Alfano, *Opt. Lett.* **18**, 241 (1993).
4. M. Hee, D. Huang, E. Swanson, J. Fujimoto, *ibid.*, p. 950.
5. D. A. Benaron and D. K. Stevenson, *Science* **259**, 1463 (1993).
6. H. Chen *et al.*, *Opt. Lett.* **16**, 487 (1991).
7. M. Duncan, R. Mahon, L. Tankersley, J. Reintjes, *ibid.*, p. 1868.
8. B. Das, K. Yoo, R. Alfano, *ibid.* **18**, 1092 (1993).
9. K. M. Yoo, B. B. Das, R. Alfano, *ibid.* **17**, 958 (1992).
10. X. Liang, L. Wang, P. Ho, R. Alfano, in preparation.
11. L. Wang, P. Ho, R. Alfano, *Appl. Opt.* **32**, 5043 (1993).
12. M. S. Patterson, B. Chance, B. C. Wilson, *ibid.* **28**, 2331 (1989).
13. F. Liu, K. M. Yoo, R. R. Alfano, *Opt. Lett.* **18**, 432 (1993).
14. H. van Staveren, C. Moes, J. van Marle, S. Prael, M. van Gemert, *Appl. Opt.* **30**, 4507 (1991).
15. Supported by grants from Medicisence Technology Corporation and the New York State Science and Technology Foundation.

8 February 1994; accepted 12 May 1994

The X-ray Surface Forces Apparatus: Structure of a Thin Smectic Liquid Crystal Film Under Confinement

Stefan H. J. Idziak, Cyrus R. Safinya, Robert S. Hill, Keith E. Kraiser, Marina Ruths, Heidi E. Warriner, Suzi Steinberg, Keng S. Liang, Jacob N. Israelachvili

An x-ray surface forces apparatus for simultaneously measuring forces and structures of confined complex fluids under static and flow conditions is described. This apparatus, combined with an intense synchrotron x-ray source, allows investigation of molecular orientations within a thin liquid crystal film confined between two shearing mica surfaces 3900 angstroms apart. The layer-forming smectic liquid crystal 8CB (4-cyano-4'-octylbiphenyl) adopted a series of distinct planar layer orientations, including the bulk flow-forbidden *b* orientation.

Confinement of complex fluids between two surfaces or in narrow pores is known to strongly alter the collective structure of the trapped molecules in molecular aggregates such as polymers, vesicles, biomembranes, or colloidal particles suspended in the liquid (1–6). Molecular dynamics simulations (7) indicate that increasing confinement may change the density and positional order, in addition to the molecular orientational order of molecules and aggregates, especially as the decreasing gap size approaches an inherent length scale, such as the diameter of suspended colloidal particles or the radius of gyration of dissolved polymer coils, or ultimately, the diameter of the trapped solvent molecules themselves.

Structural rearrangements within complex fluid systems may also be induced by flow (8–13), but such flow-induced effects do not require confinement and occur throughout the bulk fluid, for example,

when bulk nematic (10) or smectic (11) liquid crystals are sheared (Fig. 1). Another important difference between confinement-induced and flow-induced effects is that the former produce equilibrium whereas the latter produce nonequilibrium structures.

The effects of confinement on molecular conformations and transport, as well as the phase behavior of liquids in small pores

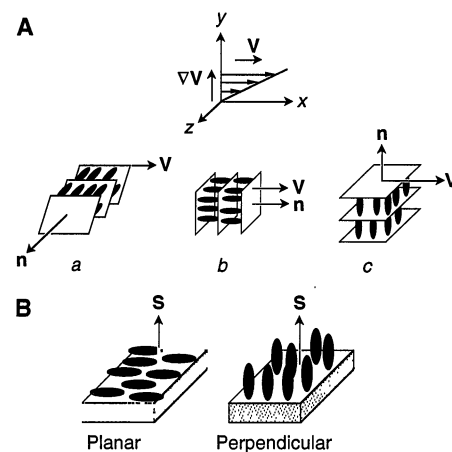


Fig. 1. (A) Definitions of the real space layer orientations during flow, following the notation of Miecawicz (23): (a) The layer normal \mathbf{n} is along the z direction; (b) the layer normal is along the velocity \mathbf{v} direction; (c) the layer normal is along the velocity gradient ($\nabla\mathbf{v}$) direction. In orientations a and c, the velocity is in the plane of the layers. (B) Planar and perpendicular (homeotropic) orientations for the liquid crystal molecules at the solid interface.

S. H. J. Idziak and K. E. Kraiser, Materials Department and the Materials Research Laboratory, University of California, Santa Barbara, CA 93106, USA.

C. R. Safinya and H. E. Warriner, Physics Department, Materials Department, and the Material Research Laboratory, University of California, Santa Barbara, CA 93106, USA.

R. S. Hill and S. Steinberg, Department of Chemical Engineering, University of California, Santa Barbara, CA 93106, USA.

M. Ruths, Chemistry Department, University of California, Santa Barbara, CA 93106, USA.

K. S. Liang, Exxon Research and Engineering Company, Annandale, NJ 08801, USA.

J. N. Israelachvili, Department of Chemical Engineering, Materials Department, and the Materials Research Laboratory, University of California, Santa Barbara, CA 93106, USA.

(with a pore size distribution), have recently been studied with spectroscopic (5), calorimetric (6), and neutron scattering techniques (14). At the true molecular level, the surface forces apparatus (SFA) technique has allowed for direct force, friction, and rheological measurements of liquid films (1–3). However, to the best of our knowledge, before the present work, liquids confined between two parallel surfaces with precisely controllable separations have not been studied with a direct imaging probe such as x-ray or neutron scattering. The in situ imaging technique we describe is a noninvasive probe of the structure and the molecular orientations of the confined system over domain sizes ranging from nanometers to micrometers. Other microscopic probes, such as atomic force microscopy, scanning tunneling microscopy, or electron microscopy, which are extremely powerful structural probes when only one surface is studied, would be invasive because of the presence of the two confining surfaces in the SFA. One would have to freeze, quench, and fracture the sample to image the exposed surface.

Here, we report synchrotron x-ray scattering structural studies with our x-ray surface forces apparatus (X-SFA) in the “mesoscale” size range, which spans the regime between about 100 and 10,000 Å. An understanding of the properties of such complex fluid systems is of fundamental scientific interest and also of importance to many technological fields, such as lubrication, the flow of colloidal and biocolloidal particles through narrow membranous or biological pores, and the processing of ceramic and polymer composite materials and films. The X-SFA is ideally suited for directly probing such mesoscale structures under both quiescent and dynamic flow conditions.

In the bulk or in thick films, where surface boundary effects are less important, the flow-induced layer orientation of the liquid crystal 4-cyano-4'-octylbiphenyl (8CB) confined between two shearing surfaces with a gap size of order 1 mm ($10^3 \mu\text{m}$) was previously measured by synchrotron x-ray scattering (10, 11). At room temperature in the smectic-A phase, the cigar-shaped 8CB molecules segregated into layers. During bulk flow, the stacked layers were parallel to the flow direction, in the so called *a* or *c* orientations (Fig. 1A). Also, liquid crystals become oriented at solid surfaces (4, 15). The two most common orientations are the “planar” and “homeotropic” orientations, where the molecules align parallel or perpendicular to the surfaces (Fig. 1B). On mica surfaces, cyano biphenyl molecules such as 8CB orient in the planar configuration (15), corresponding under flow to the plane defined by the *a* and *b* directions. Thus, for 8CB between two

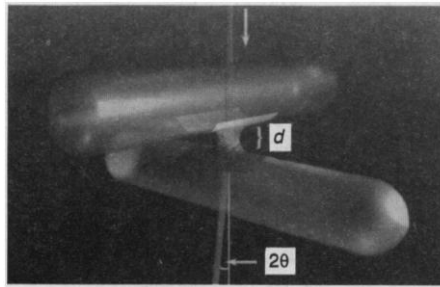


Fig. 2. Schematic of the two crossed capillary tubes used in the X-SFA designed for in situ structural studies of complex fluids under confinement and flow. The x-ray path is shown in transmission through the sample of thickness *d* as the beam scatters at an angle 2θ with respect to the incident direction.

shearing mica surfaces, confinement and flow are expected to have competing layer-orienting effects, where the relative importance of the two effects is controlled by the experimental conditions of gap thickness and shear rate.

The X-SFA is based on a conventional SFA (Mk III model) (16), which was modified for simultaneous on-line use with an intense synchrotron x-ray beam passing through or between the surfaces. In this device, the gap thickness between two atomically smooth surfaces can be adjusted from a few angstroms to $>10 \mu\text{m}$, with control to $\pm 1 \text{ \AA}$, by means of a four-stage mechanism consisting of a coupled micrometer, differential micrometer, differential spring, and piezoelectric crystal. The surfaces typically used are mica sheets in a crossed-cylinder geometry with diameters of order 2 to 5 cm, although in the experiments reported here, smaller diameters were used (Fig. 2). The curvature allows the surfaces to be brought into a single point contact. The X-SFA was mounted onto a Huber four-cycle diffractometer with an xyz translation stage that allowed the contact area between the two surfaces to be positioned at the center of rotation of the four-cycle. The xyz displacements have a range of $\pm 1 \text{ cm}$, controllable to $3 \mu\text{m}$, in each direction.

We used two 2-mm-diameter quartz capillary tubes with a wall thickness of 0.01 mm to support the mica sheets. Such thin-walled quartz glass tubes are necessary for x-ray diffraction experiments in the transmission mode, where the beam must pass through the two glass supports as well as through the sample. The cylinders were 10 mm long and were flame-sealed at both ends to improve rigidity. Back-silvered mica sheets were glued onto each cylinder to provide smooth surfaces for the measurements. The cylinders were then mounted in the X-SFA at 45° to the shear direction to enable x-ray access either in the transmission mode (beam passing through the surfaces) or reflection mode (beam passing between the surfaces). We monitored the gap

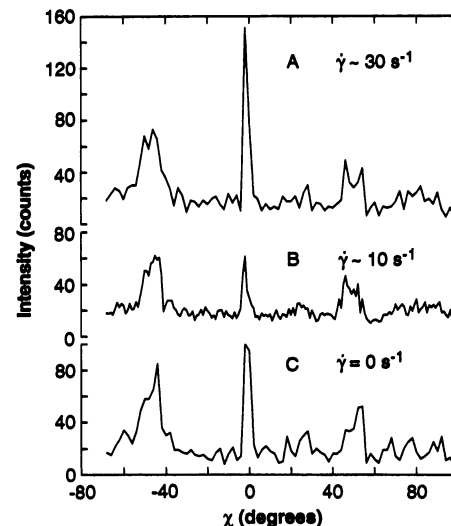


Fig. 3. The x-ray orientational scans showing the discrete planar molecular configurations at shear rates (curve A) $\dot{\gamma} = 30 \text{ s}^{-1}$, (curve B) $\dot{\gamma} = 10 \text{ s}^{-1}$, and (curve C) $\dot{\gamma} = 0 \text{ s}^{-1}$ (cylinders are stationary). The *a* orientation (Fig. 1) corresponds to $\chi \approx \pm 90^\circ$; the *b* orientation, to $\chi \approx 0^\circ$. The shearing velocity was in the plane of scattering at $\chi \approx 0^\circ$. Each point was counted for about 17 s. The point spacing in curve B is 1° , whereas the point spacing in curves A and C is 2° .

between the two cylinders by observing the pattern of Newton's rings created by passing sodium light through the two cylinders; the rings are visible because the sample is very thin. Horizontal shearing of the samples was performed through the use of a special piezoelectric bimorph lateral sliding device (16). A triangular wave voltage profile was applied to the device, which created a tangential velocity of one cylinder with respect to the other.

The measurements were conducted on beamline 10-2 at the Stanford Synchrotron Radiation Laboratory, with the intense 31-pole wiggler x-ray source. A Si(111) monochromator was used at 8 keV with the beam focused at the sample position. A $125\text{-}\mu\text{m}$ pinhole was placed several centimeters in front of the sample to define the spatial extent of the beam. The diffraction patterns were measured with a Bicron scintillation detector. A combination of slits on the diffractometer yielded a longitudinal in-plane resolution of $\delta q_{\parallel} = 0.003 \text{ \AA}^{-1}$ and an out-of-plane resolution of $\delta q_{\perp} = 0.02 \text{ \AA}^{-1}$ (full width at half maximum). Details of the x-ray spectrometer have been described elsewhere (17).

For the measurements presented below, the separation between the two surfaces was kept at 3900 \AA (18). This is the minimum spacing between the two surfaces; because of the curvature of the cylinders and the $125 \mu\text{m}$ diameter of the incident x-ray beam, the actual spacing seen by the beam ranges from 3,900 to $23,000 \text{ \AA}$.

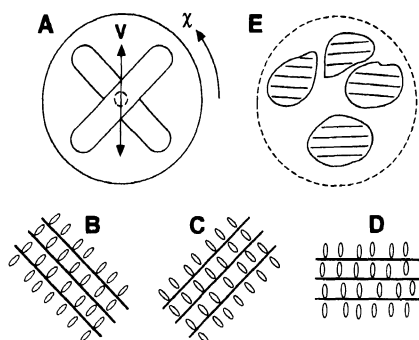


Fig. 4. Orientation of the smectic layers of 8CB between the crossed cylinders of the X-SFA as determined from the orientational scans shown in Fig. 3. (A) Sketch of the two crossed cylinders, showing the shear direction as well as the orientation angle χ . (B) The peak at $\chi = -45^\circ$ corresponds to the smectic layers lying parallel to the top cylinder, and (C) the peak at $\chi = 45^\circ$ corresponds to layers parallel to the bottom cylinder. (D) The peak at $\chi = 0^\circ$ is attributable to the layers taking up the b orientation. (E) The scattering seen in Fig. 6 implies a number of discretely oriented domains are present in the sample.

For our first series of experiments, 8CB was chosen because, as described above, its bulk structure and orientation under flow has been characterized (10, 11) and a direct comparison was desired to differentiate between flow and confinement effects on the collective molecular structure in thin films. To perform the diffraction measurements (Fig. 3), we set the detector at a scattering angle $2\theta = 2.8^\circ$, which corresponds to the 8CB layer spacing of 31.73 \AA . The incident x-ray beam was passed radially through both cylinders in the transmission mode (Fig. 2). The X-SFA was then rotated about the incident beam through an angle χ (Fig. 4A).

Considerable alignment occurs between the two crossed cylinders (Fig. 3). In addition, there is no large qualitative change in the smectic layer orientation between the case of no shear (curve C) and the highest shear rate $\dot{\gamma} = 30 \text{ s}^{-1}$ studied (curve A). The peak at $\chi = -45^\circ$ corresponds to the smectic layer normal \mathbf{n} pointing along the lower cylinder axis (Fig. 4B). Likewise, the peak at $\chi = +45^\circ$ corresponds to the layer normal pointing along the upper cylinder axis (Fig. 4C). The peak at $\chi = 0^\circ$ is attributable to the layers orienting such that the layer normal is pointing along the shear direction, that is, in the b orientation (Fig. 4D). This b orientation was not observed in the case of large gap flow studies in the smectic-A phase as it tends to tilt the layers, which is energetically costly (11). As can be seen, the effects of confinement dominate flow-induced bulk layer orientational ordering in the explored shear rate regime.

There was little or no evidence of any

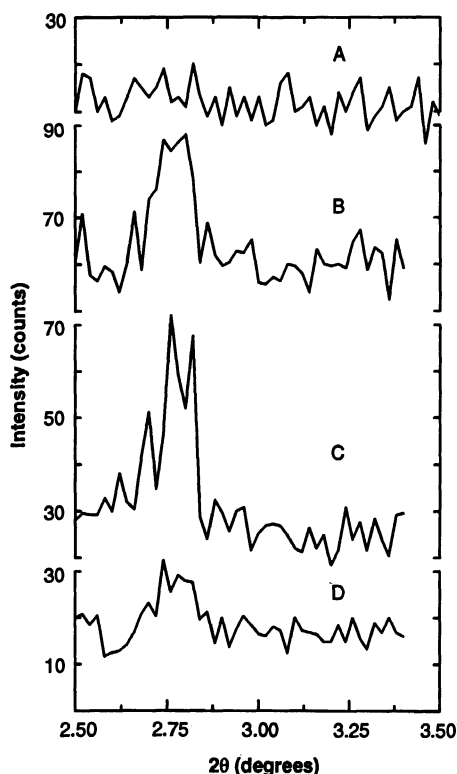


Fig. 5. Longitudinal x-ray scans along the smectic layer normal direction showing that the orientational order scans seen in Fig. 3 are indeed attributable to the smectic layers. The layer spacing of 31.73 \AA observed in bulk 8CB corresponds to a diffraction angle of $2\theta = 2.799^\circ$. (Curve A) No peak is seen for $\dot{\gamma} = 0.15 \text{ s}^{-1}$ in the c orientation. The longitudinal scans through the peaks at $\chi = -45^\circ$ (curve B), $\chi = 0^\circ$ (curve C), and $\chi = 45^\circ$ (curve D) shown in curve B of Fig. 3 for $\dot{\gamma} = 10 \text{ s}^{-1}$ demonstrate that this orientational order is coming from the smectic layers. Each point is counted for about 17 s, and the point spacing is 0.1° .

smectic layer a orientation at zero shear; this would be manifested by the observation of peaks at $\chi = \pm 90^\circ$ in curve C of Fig. 3. However, as the shear rate is increased, a broad peak appears to emerge at $\chi \approx 80^\circ$, indicating the onset of the a orientation seen in the bulk (11).

Longitudinal scans through the peaks at $\chi = -45^\circ$, 0° , and 45° in curve B of Fig. 3 (Fig. 5, curves B through D) demonstrate that the observed orientational ordering seen in the X-SFA is attributable to the ordering of the smectic layers, which maintain their bulk layer spacing of 31.73 \AA . In a longitudinal scan through the c orientation (Fig. 5, curve A), the incident x-ray beam passes between the two cylinders, where it scatters into the detector (reflection mode). This scan shows that there is no observable c orientation present in the smectic under flow.

We made a more detailed measurement of the b orientation of Fig. 3 (close to $\chi = 0^\circ$) (Fig. 6). The data point spacing was decreased to show the fine structure present

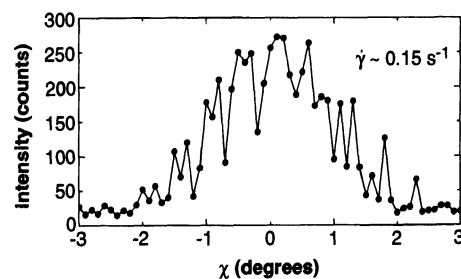


Fig. 6. Orientational scan showing the fine structure of the peak at $\chi = 0^\circ$ for $\dot{\gamma} = 0.15 \text{ s}^{-1}$. This shows that a discrete set (rather than the expected continuous distribution) of layer orientations is formed. Each point was counted for about 17 s (400,000 monitor counts) and the point spacing is 0.1° .

in this peak. The b orientation does not consist of a continuous orientational distribution (that is, of a mosaic spread of orientations) centered about the expected orientation; instead, it is formed by orientationally discrete domains (Fig. 4E). In general, small numbers of widely spaced, discrete domains have been observed in highly aligned liquid crystalline samples, such as smectic thin films (19) and discotic strands (20). However, the sample confined between the surfaces of the X-SFA exhibits a large number of closely spaced discrete orientations where the orientational spacing between domains is of order the mosaic width of each domain. The overall angular width of the b peak of 3.6° is about the same as the angular variation of the surfaces that are illuminated by the beam; the $125\text{-}\mu\text{m}$ x-ray beam illuminates $1/50$ of the cylinder circumference, or 7° .

The results demonstrate that the X-SFA is a noninvasive technique capable of imaging structures and orientations in confined complex fluids. The method opens up the path for the simultaneous measurement of forces and microstructures of simple or complex liquids in confined geometries under static and nonequilibrium flow conditions. This first set of measurements in the mesoscale gap regime were made feasible through the combination of the well-developed methodology of the SFA and an intense x-ray source emanating from a wiggler beam line. Structural measurements of confined liquids at the true molecular level, which require small x-ray beam sizes (21), will be tremendously facilitated at third-generation synchrotron facilities (22) with extremely high-brilliance x-ray beam sources with cross-sectional areas of order $10 \text{ }\mu\text{m}$.

REFERENCES AND NOTES

1. J. N. Israelachvili, *Intermolecular and Surface Forces* (Academic Press, New York, ed. 2, 1991).

2. J. Van Alsten and S. Granick, *Phys. Rev. Lett.* **61**, 2570 (1988).
3. J. Klein, D. Perahia, S. Warburg, *Nature* **352**, 143 (1991); J. N. Israelachvili, A. M. Homola, P. M. McGuiggan, *Science* **240**, 189 (1988).
4. J. Als-Nielsen, in *Topics in Current Physics*, W. Schommers and P. V. Blackenhagen, Eds. (Springer-Verlag, Berlin, 1987), p. 181; P. S. Pershan, *J. Phys. Colloq.* **50**, C7 1 (1989); B. Jerome, *Rep. Prog. Phys.* **54**, 391 (1991), and references therein.
5. See, for example, J. M. Drake and J. Klafter, *Phys. Today* **43**, 46 (May 1990), and references therein; J. M. Drake, J. Klafter, P. Levitz, *Science* **251**, 1574 (1991).
6. T. Bellini *et al.*, *Phys. Rev. Lett.* **69**, 788 (1992).
7. M. Schoen, D. J. Diestler, J. H. Cushman, *J. Chem. Phys.* **87**, 5464 (1987); C. L. Rhykerd Jr., M. Schoen, D. J. Diester, J. H. Cushman, *Nature* **330**, 461 (1987); P. A. Thompson, M. O. Robbins, G. S. Grest, *Phys. Rev. Lett.* **68**, 3448 (1992).
8. K. Weissenberg, *Nature* **159**, 310 (1947); R. F. Bruinsma and C. R. Safinya, *Phys. Rev. A* **43**, 5377 (1991).
9. N. A. Clark and B. J. Ackerson, *Phys. Rev. Lett.* **44**, 1005 (1980).
10. C. R. Safinya, E. B. Sirota, R. Plano, R. F. Bruinsma, *J. Phys. Condens. Matter* **2**, SA365 (1990); C. R. Safinya, E. B. Sirota, R. Plano, *Phys. Rev. Lett.* **66**, 1986 (1991).
11. C. R. Safinya *et al.*, *Science* **261**, 588 (1993).
12. O. Diat and D. Roux, *J. Phys. II* **3**, 1427 (1993).
13. K. A. Koppi, M. Tirrell, F. S. Bates, K. Almdal, R. H. Colby, *ibid.* **2**, 1941 (1992); K. A. Koppi, M. Tirrell, F. S. Bates, *Phys. Rev. Lett.* **70**, 1449 (1993).
14. N. A. Clark *et al.*, *Phys. Rev. Lett.* **71**, 3505 (1993).
15. P. Pieranski and B. Jerome, *Phys. Rev. A* **40**, 317 (1989).
16. J. N. Israelachvili and P. M. McGuiggan, *J. Mater. Res.* **5**, 2223 (1990).
17. C. R. Safinya *et al.*, *Phys. Rev. Lett.* **57**, 2718 (1986); C. R. Safinya, E. B. Sirota, D. Roux, G. S. Smith, *ibid.* **62**, 1134 (1989); G. S. Smith, E. B. Sirota, C. R. Safinya, R. J. Plano, N. A. Clark, *J. Chem. Phys.* **92**, 4519 (1990).
18. We set the gap by observing the Newton's rings pattern that resulted when sodium light was passed through the two cylinders. The 3900 Å measurement results from separating the two surfaces by two fringes from contact. By monitoring the movements of fringes of equal chromatic order, we could set the gap as accurately as 1 Å (16).
19. D. E. Moncton and R. Pindak, *Phys. Rev. Lett.* **43**, 701 (1979); J. Collet *et al.*, *ibid.* **49**, 553 (1982).
20. C. R. Safinya *et al.*, *ibid.* **53**, 1172 (1984); E. Fontes *et al.*, *Phys. Rev. A* **37**, 1329 (1988); P. A. Heiney *et al.*, *J. Phys.* **50**, 461 (1989).
21. Because of the finite curvature of the surfaces, a small beam size is required to probe ultrathin liquids of order a few molecular layers.
22. The European Synchrotron Source (ESRF) at Grenoble, France, and the Advanced Photon Source (APS) at Argonne National Laboratories.
23. M. Miecawicz, *Nature* **158**, 27 (1946).
24. We gratefully acknowledge conversations with J. Klein, N. Clark, and P. Pincus. C.R.S. and J.N.I. gratefully acknowledge partial support by the Office of Naval Research under grant N00014-93-1-0269. C.R.S. gratefully acknowledges support from the Exxon Education Foundation. The synchrotron x-ray scattering experiments were carried out at beamline 10-2 at the Stanford Synchrotron Radiation Laboratory, which is supported by the U.S. Department of Energy. The Materials Research Laboratory at Santa Barbara is supported by the NSF under grant DMR-9123048.

23 November 1993; accepted 9 May 1994

Functional Role of Type I and Type II Interferons in Antiviral Defense

Ulrike Müller, Ulrich Steinhoff, Luiz F. L. Reis, Silvio Hemmi, Jovan Pavlovic, Rolf M. Zinkernagel, Michel Aguet*†

Mice lacking the known subunit of the type I interferon (IFN) receptor were completely unresponsive to type I IFNs, suggesting that this receptor chain is essential for type I IFN-mediated signal transduction. These mice showed no overt anomalies but were unable to cope with viral infections, despite otherwise normal immune responses. Comparison of mice lacking either type I or type II IFN receptors showed that, at least in response to some viruses, both IFN systems are essential for antiviral defense and are functionally nonredundant.

Interferons were discovered on the basis of their antiviral activity. Two families of IFNs can be distinguished: type I IFNs (IFN- α , IFN- β , and IFN- ω), which are encoded by a family of over 20 genes (1), and type II IFN (IFN- γ), which is structurally unrelated and encoded by a single gene (2). In addition to their antiviral properties, type I and type II IFNs exert widely overlapping pleiotropic effects including inhibition of cell growth, antitumor action, involvement in hematopoiesis, and regulatory effects on cellular and humoral immune responses (3) which may be pathogenic in certain autoimmune diseases (4). The biological relevance of these nonantiviral effects remains elusive.

The isolation of a trophoblast IFN (IFN- ω) from ruminants revived the question of whether IFNs are also engaged in embryonic development (5).

To elucidate the physiological role of the type I IFN system, we generated mice with a deficient type I IFN system. Because inactivation of the entire type I IFN gene family was unfeasible, the gene encoding the known receptor subunit was chosen as a target. Even though type I IFNs were shown to cross-compete for receptor binding (6, 7), some evidence suggested that several type I receptors may exist (8, 9). Still, reconstitution of an IFN-resistant murine cell line with the known receptor subunit indicated that this receptor component might be essential for the response to IFN- α/β (10). Inactivation of the type I IFN receptor gene in embryonic stem (ES) cells was achieved by homologous recombination (11) as described in Fig. 1. The IFN- α/β ^{0/0} mice were obtained with a mendelian frequency, proved fertile, and had no apparent phenotypic anomalies by 6 months of age. Northern (RNA) blot analysis of total RNA from primary embryonic

fibroblasts (PMEFs) hybridized with the complete murine IFN- α/β complementary DNA (cDNA) as a probe revealed a 4.5-kb mRNA for wild-type cells (10), whereas no transcript was detected for mutant cells (12), possibly because of instability of the truncated, mutant mRNA.

As expected, the type I receptor was functionally inactive, because PMEFs from IFN- α/β ^{0/0} embryos were unresponsive to the antiviral action of natural murine type I IFN, a mixture of IFN- α and IFN- β (Fig. 2A). However, mutant cells remained sensitive to IFN- γ , although we observed one-fourth to one-eighth the sensitivity as compared with wild-type cells. Functional inactivation of the type I receptor was further confirmed by Northern blot analysis of the RNA from PMEFs with probes derived from several different IFN-inducible genes (Fig. 2B). Mutant cells were unresponsive to natural type I IFNs, recombinant murine IFN- β , and recombinant human IFN- α_2/α_1 to which normal mouse cells are responsive (13). In this assay the response to murine IFN- γ was indistinguishable from that of wild-type cells. We found no evidence for a functional alteration of the IFN- γ system in IFN- α/β ^{0/0} mice. Thus, IFN- α/β ^{0/0} mice were as resistant to *Listeria monocytogenes* as wild-type mice, whereas IFN- γ ^{0/0} mice were highly susceptible to this pathogen (14).

To monitor the response to type I IFN *in vivo*, we analyzed the induction of the *Mx-1* gene, a strictly type I IFN-specific response marker in mouse cells (15). Mutant and wild-type animals were injected intraperitoneally with either the IFN inducer poly(I). poly(C) (PIC; Fig. 2C) or recombinant human IFN- α_2/α_1 (10⁵ U), or they were infected intravenously with 2 × 10⁶ plaque-forming units (PFU) of vesicular stomatitis virus (VSV). RNA from various tissues was isolated after 7.5 hours (IFN- α_2/α_1 and PIC)

U. Müller, L. F. L. Reis, S. Hemmi, M. Aguet, Institute of Molecular Biology I, University of Zürich, Höggerberg, 8093 Zürich, Switzerland.

U. Steinhoff and R. M. Zinkernagel, Institute of Experimental Immunology, University of Zürich, 8057 Zürich, Switzerland.

J. Pavlovic, Institute of Medical Virology, University of Zürich, 8028 Zürich, Switzerland.

*To whom correspondence should be addressed.

†Current address: Genentech Incorporated, 460 Point San Bruno Boulevard, South San Francisco, CA 94080, USA.